Improvements to an Euler Aerodynamic Method for Transonic Flow Analysis

Pradeep Raj* and James E. Brennan†
Lockheed Aeronautical Systems Company, Burbank, California

Modifications to a three-dimensional Euler aerodynamic method (TEAM) and their effect on the accuracy of transonic flow simulations are described. TEAM's solution algorithm is based on a finite-volume spatial discretization and multistage time-stepping algorithm to solve the Euler equations. Treatment of numerical dissipation and surface boundary condition are specifically addressed. The modified code includes the standard adaptive dissipation scheme using blended second and fourth differences and a flux-limited dissipation scheme. Improved treatment of the surface boundary condition minimizes spurious entropy production. TEAM computations are correlated with experimental data for two wings, ONERA M-6 and Wing C, and an arrow wing-body configuration. For Wing C, the TEAM predictions are also compared with those of the full-potential TWING code on identical grids.

Introduction

ACCURATE computational simulation of three-dimensional transonic flow about complete aircraft, as well as their components, is of considerable interest to airplane designers. Computational methods based on Navier-Stokes equations[1,2] are obviously preferable. However, their routine application for aircraft design is restricted by two factors: 1) requirement of large computational time and storage; and 2) limited reliability due to the empiricism in turbulence modeling when Reynolds-averaged equations are used. Ongoing research is likely to minimize the impact of these factors in coming years.

In the interim, considerable advances have been made to solve inviscid approximations to the Navier-Stokes equations. Codes based on full-potential equations (FPE) have been used successfully to analyze wings[3,4] and wing-body configurations.[5,6] Some success has been reported in extending panel methods to analyze complete aircraft in transonic flow.[7] Because of the inherent assumptions, accuracy of potential-flow solutions deteriorates in the presence of strong shocks and regions of rotational flow. Recent advances in numerical algorithms to solve the nonlinear Euler equations[8-10] provide an attractive and cost-effective alternative.

Improvements to a three-dimensional Euler aerodynamic method (TEAM) are the subject of this paper. Their description follows an overview of the basic features of the TEAM code. The modified code is used to analyze two wings, ONERA M-6 and Wing C, and an arrow wing-body configuration. Correlations of computed results with experimental data are in the Results and Discussion section. For Wing C, the TEAM computations are also correlated with the predictions of an FPE code.

Three-Dimensional Euler Aerodynamic Method

The TEAM code is based on the explicit multistage time-stepping, finite-volume algorithm[8] to solve the Euler equations. The finite-volume formulation essentially decouples the flow solver from the grid-generation step. The grids may be constructed in any convenient manner; only the Cartesian coordinates are required by the solver. This feature has been exploited in developing the TEAM code that can be employed to analyze wing and wing-body configurations using boundary-conforming grids of C–H, C–O, O–O, or O–H topologies. Another version of the code can be used to analyze wing-body-tail (canard)-fin configurations using grids of H–H topology. The C–H topology is illustrated in Fig. 1; others may be analogously defined. The grid-generation methods used here and the basic aspects of the flow-solver algorithm are briefly described next. Additional details about the solver can be found in Refs. 8–14.

Flow Solver

TEAM's flow-solver algorithm requires that the region surrounding a given configuration be subdivided into small hexahedral cells. In each cell, the semidiscrete approximations to the time-dependent Euler equations, representing mass, momentum, and energy conservation, are integrated in time using a multistage scheme. Convergence to steady state is typically achieved in a few hundred pseudo-time steps in which the step size for each cell is determined by local stability restrictions. In contrast, thousands of steps are required when using a conventional explicit scheme with a global minimum step size. Enthalpy damping[8,15] and implicit residual smoothing[9] further reduce the number of time steps required to reach the steady state.

A cell-centered spatial discretization is used in the present algorithm, i.e., the flow variables are defined at cell centers, and the flux is computed at cell faces. It reduces to a central-difference scheme, which is formally second-order accurate for smooth grids. This scheme has to be augmented by dissipation terms (also known as artificial or numerical viscosity) in order to suppress its well-known tendency for odd-even point decoupling, to capture shocks, and to miminize pre- and postshock oscillations. The dissipation terms can be constructed in a variety of ways, two of which are included in TEAM. Appropriate nonreflecting boundary conditions are used at the far-field boundaries.[9,13] A no-normal-flow condition is imposed on the solid surface. A precise treatment of this condition and associated improvement in accuracy is described later.

A typical solution starts with initialization of flow variables, namely density, three Cartesian components of momentum, static pressure, and total energy, in all the cells either to the

Presented as Paper 87-0040 at the AIAA 25th Aerospace Sciences Meeting, Reno, NV, Jan. 12–15, 1987; received Feb 26, 1987; revision received April 17, 1987.

*Research and Development Engineer, Computational and Advanced Aerodynamics Department. Member AIAA.

†Senior Aerodynamics Engineer, Computational and Advanced Aerodynamics Department. Member AIAA.

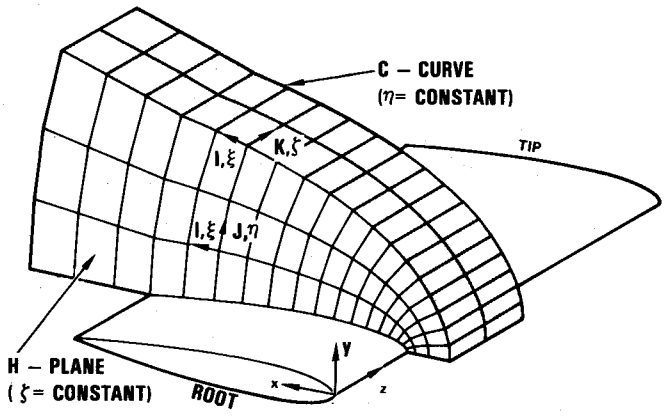

Fig. 1 C–H grid topology.

freestream conditions or to user-supplied data. Following each time step, the ratio of the current average residual (the root-mean-square value of net mass flux) and its initial value are checked against a user-supplied convergence criterion to determine whether the steady-state solution has been reached. Typically, a three- to four-orders-of-magnitude reduction yields answers of engineering accuracy. The time marching stops either when the convergence criterion is met, or after a prescribed number of steps. The solution may be restarted, if desired, to perform additional steps.

Grid Generation

For the present investigation, two methods were used to generate the required grids. An O–H grid about Wing C was generated using the method built into the TWING code.[4] In this technique, three-dimensional grids about wings are constructed by suitable interpolation of two-dimensional grids at selected wing cross sections. The two-dimensional sectional O-type grids are generated by solving elliptic partial differential equations. Its approximate factorization algorithm leads to a computationally efficient procedure.

For both the wings and the arrow wing-body configuration, the Parabolic Conformal Mapping with Shearing (PACMAPS) code was used to generate C-H grids. This code relies on a sequence of conformal transformations with shearing to map the bounding surfaces in the physical domain to a rectangular mapped domain. The points of intersection of the coordinate lines in the mapped domain define the nodal points of the grid. The corresponding Cartesian coordinates are obtained by inverting the transformations. This code incorporates the basic methodology of the FLO-28[5] and FLO-59[9] codes with modifications for enhanced capabilities. Appropriate stretching functions have been incorporated to control the shape and location of the far-field boundary, an especially useful feature in generating grids about highly tapered wings. An added measure of user-friendliness is provided by the automatic computation of singular points (about which wing sections are unwrapped) for wings having round as well as sharp leading edges. A user can also cluster points in regions of interest, e.g., near leading-edge or wing-tip or wing-body junctions, by varying only a few parameters in the input data sets. The method is fast and easy to use.

Improvements to TEAM Flow Solver

Flux Computation

One of the changes incorporated into the TEAM code involves the evaluation of the flux term in the Euler equations:

$$\frac{\partial}{\partial t}\int_{\Omega} Q\,\mathrm{d}\Omega + \int_{A} \bar{F}\cdot\hat{n}\,\mathrm{d}A = 0 \tag{1}$$

where

$$Q = \begin{bmatrix} \rho \\ \rho u_i \\ \rho E \end{bmatrix}$$

Here, ρ denotes density, u_i are Cartesian velocity components, E is total energy, and A is area of the surface enclosing volume Ω.

In the original version of the algorithm, the flux defined by the second term on the left-hand side in Eq. (1) was approximated by

$$\bar{F}\cdot\hat{n} = \begin{bmatrix} \rho(u_j n_j) \\ (\rho u_i)(u_j n_j) \\ (\rho H)(u_j n_j) \end{bmatrix} + \begin{bmatrix} 0 \\ p n_j \delta_{ij} \\ 0 \end{bmatrix} \tag{2}$$

Values of density, velocity components, total enthalpy ($H = E + p/\rho$), and static pressure p at a cell face were obtained by averaging the corresponding values in neighboring cells. The standard summation notation is used in writing Eq. (2).

An alternative approximation has been incorporated into the present code. It is given by

$$\bar{F}\cdot\hat{n} = \begin{bmatrix} (\rho u_j) n_j \\ (\rho u_i u_j + p\delta_{ij}) n_j \\ (\rho u_j H) n_j \end{bmatrix} \tag{3}$$

The quantities in parentheses are averaged from the neighboring cells to determine the values at cell faces.

For smooth flows, the two formulations give essentially identical results. Even for flows with shocks, the differences in results are rather insignificant. However, the modified procedure given by Eq. (3) has the desirable property of providing correct jump conditions across a shock aligned with the cell face. The modified procedure was used for all the results presented in this paper.

Adaptive Dissipation Near Boundaries

An adaptive dissipation formulation using blended second and fourth differences in each of the three parametric directions was proposed by Jameson et al.[8] as a suitable model for the numerical dissipation. For a typical cell face separating two adjacent cells identified by (i, j, k) and $(i, j+1, k)$ set of indices, the dissipative flux term is written as

$$d_{i,j+1/2,k} = \varepsilon_2 \cdot e_{i,j+1/2,k} - \varepsilon_4 \cdot (e_{i,j+3/2,k} - 2e_{i,j+1/2,k} + e_{i,j-1/2,k}) \tag{4}$$

where

$$e_{i,j+1/2,k} = \alpha(Q_{i,j+1,k} - Q_{i,j,k})$$

$$\alpha = (\Lambda_{i,j+1,k} + \Lambda_{i,j,k})/2$$

$$\Lambda_{i,j,k} = (\lambda^i + \lambda^j + \lambda^k)_{i,j,k}$$

Here, λ^i, λ^j, and λ^k are estimates of the spectral radii of the flux-Jacobian matrices in the i, j, and k directions, respectively. Note that the subscripts refer to a spatial location, either cell center or cell face, and the superscript denotes the index direction. The first part of Eq. (4) contains the first difference of the dependent variables, and the second part is equivalent to the third difference. The net contribution in the j direction is then expressed as

$$D^j_{i,j,k} = d_{i,j+1/2,k} - d_{i,j-1/2,k}$$

which contains second and fourth differences. Similar expressions can be written for net contributions in the i and k direc-

ORDER OF APPROXIMATION

SCHEME \ CELL	1	2	⩾ 3
A	(ZERO FLUX)	2ND	2ND + 4TH
B	2ND	2ND + 3RD	2ND + 4TH
C	1ST + 2ND	2ND + 3RD	2ND + 4TH
D	2ND + 3RD	2ND + 4TH	2ND + 4TH

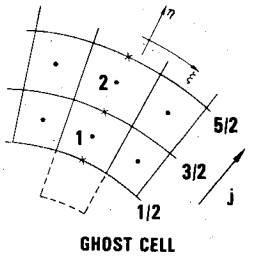

Fig. 2 Order of approximation of dissipation terms in normal direction near solid surfaces for four schemes.

tions. Then, the total dissipation flux for the (i,j,k) cell is

$$D_{i,j,k} = (D^i + D^j + D^k)_{i,j,k} \tag{5}$$

The net dissipation flux defined by Eq. (5) is appended to the right-hand side of the discretized form of Eq. (1).

A user-specified coefficient VIS-2, scaled by the normalized magnitude of the second derivative of static pressure, is used to define ε_2. This introduces a larger amount of dissipation where it is needed the most—near shocks and stagnation points—to suppress wiggles and overshoots. Another user-input coefficient, VIS-4, divided by 64, defines ε_4. The fourth-difference terms are turned off in regions where their values are smaller than those of the second-difference terms. The input values of VIS-2 and VIS-4 are typically of order one.

For cells near the boundaries, the expressions in Eq. (4) obviously cannot be used. Different formulations for these terms introduced errors into the solution leading to a boundary-layer type of behavior.[16] In an attempt to get a better understanding of the numerical-dissipation treatment near the boundary and its effect on the accuracy of the solution, four different schemes were used. The corresponding order of approximation of the dissipation terms in the local normal direction is summarized in Fig. 2.

Scheme A

The dissipative fluxes at the boundary face ($j = 1/2$) and at the $j = 3/2$ face are approximated as follows:

$$d_{i,1/2,k} = d_{i,3/2,k}$$

$$d_{i,3/2,k} = \varepsilon_2 e_{i,3/2,k} - \varepsilon_4(e_{i,7/2,k} - 2e_{i,5/2,k} + e_{i,3/2,k})$$

As a consequence, the contribution of the j direction terms in the first cell ($j = 1$) adjacent to the boundary surface is turned off. This scheme was in the version of the FLO-57 code used as the starting point for TEAM development.

Scheme B

In this scheme, the first difference at the $j = 1/2$ cell face adjacent to the boundary is approximated by its value at the opposite face (at $j = 3/2$), and the third difference is set to zero, i.e.,

$$d_{i,1/2,k} = \varepsilon_2 e_{i,3/2,k}$$

$$d_{i,3/2,k} = \varepsilon_2 e_{i,3/2,k} - \varepsilon_4(e_{i,5/2,k} - e_{i,3/2,k})$$

Scheme C

The formulation of this scheme is similar to the noncentered differences proposed by Rizzi and Eriksson.[17] It differs only slightly from scheme B. At the $j = 1/2$ face, the first difference is also set to zero, which results in a globally conservative scheme.

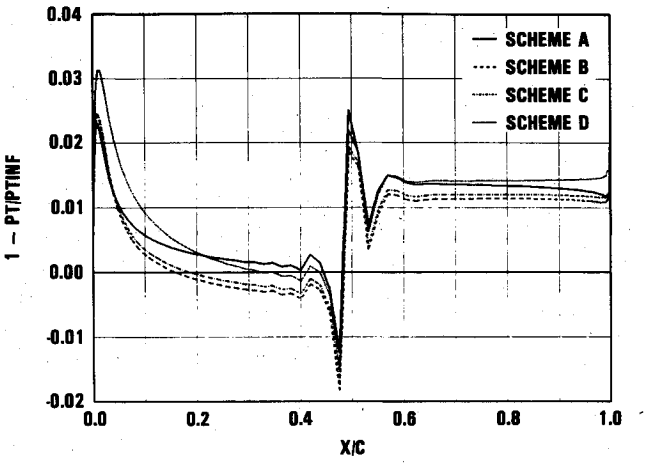

Fig. 3 Effect of dissipation schemes on surface pressure for NACA 0012 airfoil, $M = 0.8$, $\alpha = 0$ deg, 161 × 33 O grid.

Scheme D

The dissipation terms for this scheme are constructed using a ghost cell as proposed by Salas et al.[16] The flow variables in the ghost cell are obtained from the interior cell using the reflection condition. The dissipative flux at the boundary face is expressed as

$$d_{i,1/2,k} = \varepsilon_2 e_{i,1/2,k} - \varepsilon_4(e_{i,3/2,k} - e_{i,1/2,k})$$

To evaluate the sensitivity of the solution to these schemes, the NACA 0012 airfoil and Wing C were considered. The findings are summarized as follows.

NACA 0012

The airfoil was analyzed at 0.8 Mach number and zero angle of attack using an O grid with 33 O curves, each defined by 161 nodes. The computed lift coefficient was zero for all cases. A comparison of the drag coefficient C_d and surface pressure distributions showed that the results for schemes B, C, and D were essentially identical but that they all differed a little from those of scheme A. The value of C_d using scheme A was 0.0003 less than 0.0088 obtained using others. For all cases, VIS-2 was set to 0.25 and VIS-4 to 1.0. None of the schemes emerged as clearly superior to others, even after scrutiny of the surface total pressure loss distributions shown in Fig. 3. The total pressure is defined as

$$p_T = p[1 + (\gamma - 1)(M^2/2)]^{\gamma/(\gamma-1)}$$

where p is static pressure, M the Mach number, and γ the ratio of specific heats. The cause of relatively large losses near the leading edge was traced to the surface boundary condition treatment, as discussed later.

Wing C

Wing C was analyzed at 0.85 Mach number and 5 deg angle of attack using a 129 × 25 × 25 C-H grid. The computed surface pressure distributions corresponding to the four schemes were compared with each other and with the experimental data. As shown in Fig. 4, the results exhibit an increased sensitivity to the dissipation schemes compared to the airfoil case. For schemes B, C, and D, the results are in good agreement with each other, but they all differ from those of scheme A. This disparity is due primarily to the different treatment of dissipation in the first row of cells ($j = 1$) along the branch cuts aft of the wing trailing edge and outboard of the tip. In scheme A, the contribution in the local normal index direction is ignored, whereas it is included in all other schemes. Overall, the computed results for schemes B, C, and D are in closer agreement with the measured ones than those for scheme A.

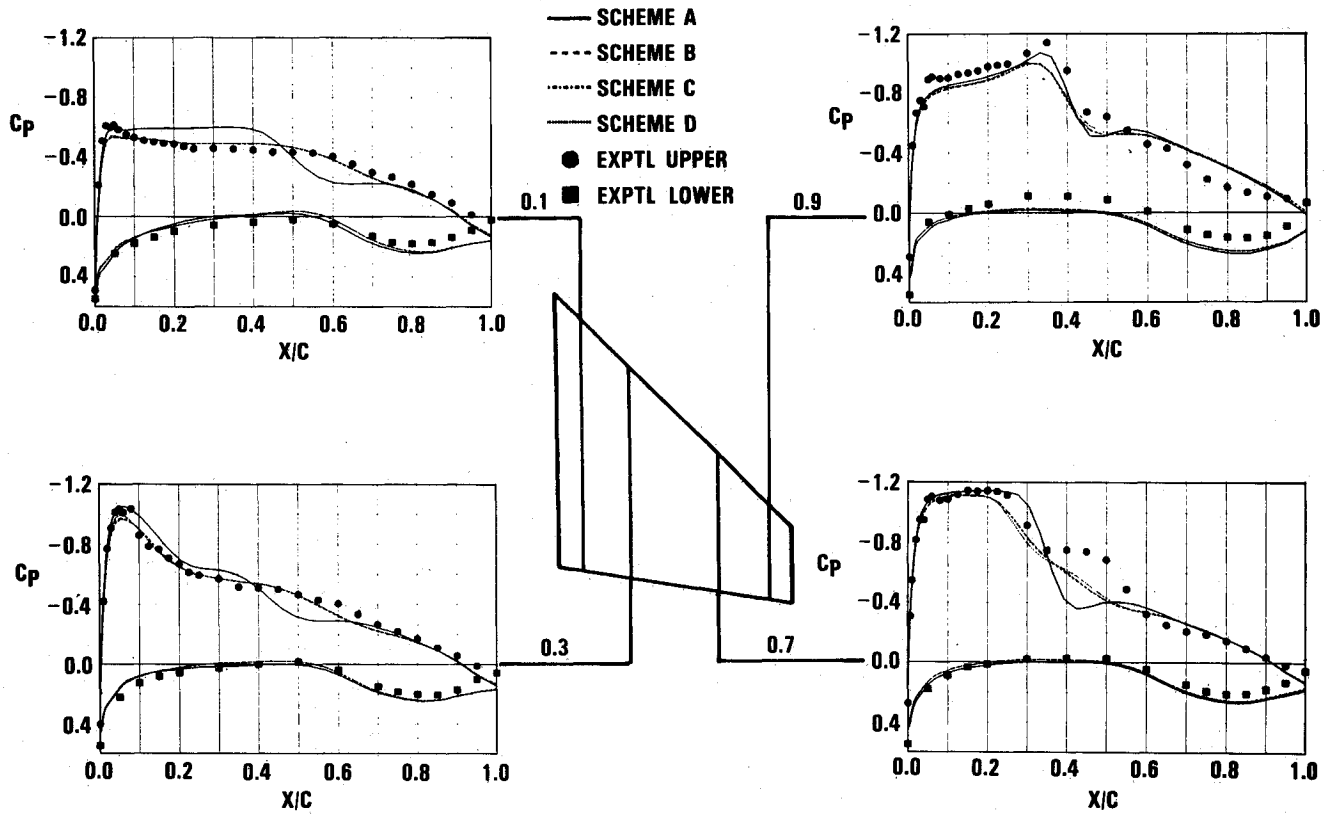

Fig. 4 Effect of numerical dissipation schemes on total pressure loss variation for NACA 0012 airfoil, $M = 0.8$, $\alpha = 0$ deg, 161 × 33 O grid.

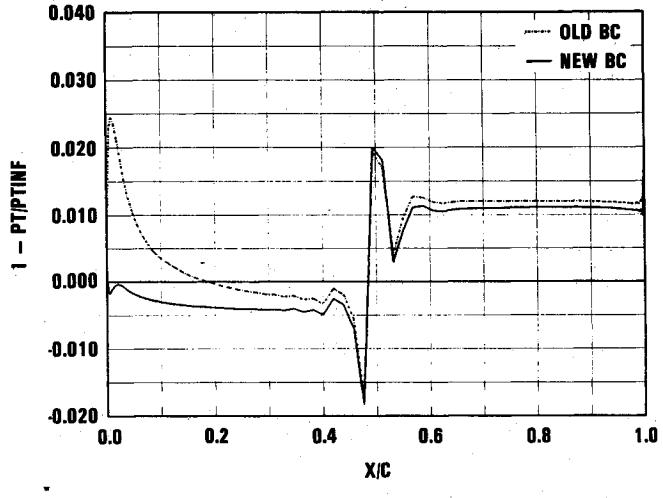

Fig. 5 Effect of numerical dissipation schemes on computed surface pressure distributions for Wing C, $M = 0.85$, $\alpha = 5$ deg, 129 × 25 × 25 C–H grid.

Scheme C, although formally lower-order accurate near the boundaries, was selected for the computations reported in this paper. This selection was guided by the global conservation and global dissipation[17] properties of this scheme.

Surface Boundary Condition

On a solid surface, the no-normal-flow condition is imposed by setting the convected flux—terms containing velocity components in Eq. (3)—to zero for all faces abutting the surface. Only the pressure on such a face contributes to the momentum flux balance. Because pressure is calculated at the center of the cell, its value at the surface itself has to be estimated. The surface value is obtained using the cell-center value and the pressure gradient at the surface. The latter is obtained by solving the normal momentum equation at the surface:

$$\rho \bar{V} \cdot (\bar{V} \cdot \nabla)\hat{n} = \hat{n} \cdot \nabla p \tag{6}$$

Here, ρ is density, p is static pressure, and $\bar{V}$ is the velocity vector. Numerical implementation of this equation requires estimates of metric quantities and flow variables, namely density and velocity, on the surface. One of the simplest approximations is to use cell-center values as is done in the FLO-57 code. This treatment was used for the results of Fig. 3.

In attempts to implement Eq. (6) more precisely, the metric quantities on the surface were estimated using central and one-sided differences. For estimating the flow variables, several options were tried:

1) Taylor series expansion about the cell center.[18]
2) Lagrange two-point interpolation formula along the local normal direction.
3) Averaging the values in the interior and ghost cells, where the latter are obtained using reflection condition.

None of these options gave totally satisfactory results, especially near the leading-edge region. Although their effect on the computed surface pressure was minimal, estimates for surface Mach number were quite different for the different options.

The following modification has largely rectified the problem. The surface density is now obtained using the condition of zero normal derivative of entropy. The surface velocity components are obtained by reflecting the contravariant velocity components, subject to the stipulation that the normal component be zero at the surface. The resulting velocity components are scaled to ensure that the total enthalpy is constant. The effect of this formulation on the total pressure loss on the surface is shown in Fig. 5.

Flux-Limited Dissipation

The standard adaptive dissipation scheme using blended second and fourth differences is quite effective in suppressing os-

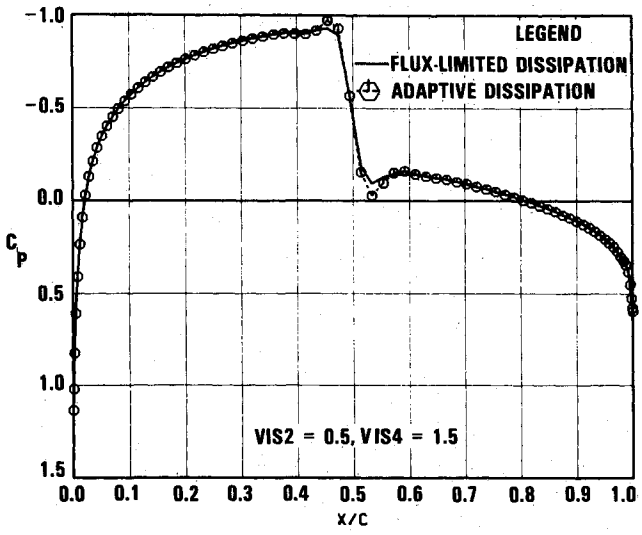

Fig. 6 Effect of surface boundary condition treatment of total pressure loss variation for NACA 0012 airfoil, $M = 0.8$, $\alpha = 0$ deg, 161 × 33 O grid.

cillations in the neighborhood of shock waves. However, some pre- and postshock oscillations may be present unless the input value of the VIS-2 coefficient is fine-tuned. It has long been known that upwind differencing eliminates spurious oscillations, albeit at increased computational effort resulting from characteristic decompositions. Jameson[19] developed an alternative formulation using flux limiters that is computationally as efficient as the standard adaptive scheme. In the case of a scalar conservation law, this formulation leads to a total variation diminishing scheme provided that the coefficients are appropriately chosen. For this scheme, a typical dissipative flux term at a cell face is expressed as

$$d_{i,j+1/2,k} = B(e_{i,j+3/2,k}, e_{i,j+1/2,k}) - 2e_{i,j+1/2,k} + B(e_{i,j+1/2,k}, e_{i,j-1/2,k}) \quad (7)$$

where

$$e_{i,j+1/2,k} = \alpha(Q_{i,j+1,k} - Q_{i,j,k})$$

$$\alpha = \beta(\lambda^j_{i,j,k} + \lambda^j_{i,j+1,k})/2$$

$$B(a,b) = [s(a) + s(b)]\min(|a|,|b|)$$

$$s(a) = 1/2, \quad a \geq 0$$

$$= -1/2, \quad a < 0$$

As recommended by Jameson,[19] β is constructed using two user-specified parameters, VIS-2 and VIS-4. The value of VIS-4 determines a threshold, and the value of VIS-2 (which is scaled by the pressure gradient analogous to the adaptive dissipation scheme) is selected to insure enough dissipation to suppress oscillations in the neighborhood of shocks. The solutions are not found to be very sensitive to these parameters, as shown by the results presented later.

The TVD property of the flux-limited dissipation scheme is clearly illustrated in Fig. 6, where surface pressure distributions on the NACA 0012 airfoil computed using adaptive and flux-limited dissipation are compared. The corresponding total pressure losses on the surface are compared in Fig. 7.

Results and Discussion

In this section, correlations of computed and experimental results for the ONERA M-6 wing, Wing C, and an arrow wing-body configuration are presented. For Wing C, TEAM

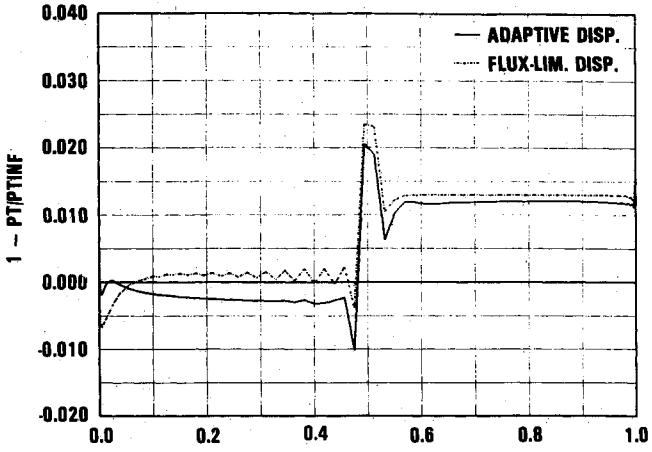

Fig. 7 Comparison of computed pressure distributions using adaptive and flux-limited dissipation for NACA 0012 airfoil, $M = 0.8$, $\alpha = 0$ deg, 161 × 33 O grid.

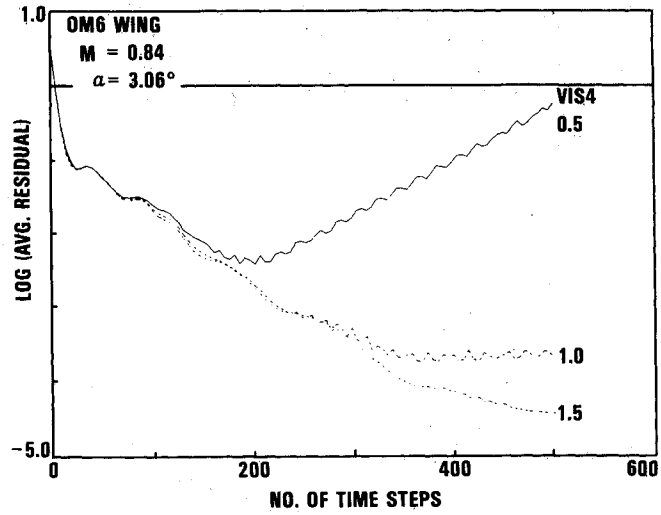

Fig. 8 Effect of numerical dissipation parameter on convergence for ONERA M-6 Wing, $M = 0.84$, $\alpha = 3.06$ deg, 129 × 29 × 33 C-H grid.

results are also correlated with those of TWING[4] on identical grids. For all cases, the flowfield is initialized to freestream conditions, and no Kutta condition is explicitly applied.

ONERA M-6 Wing

The first set of results are for the well-known ONERA M-6 wing,[20] with an aspect ratio of 3.8, a taper ratio of 0.56, and a leading-edge sweep of 30 deg. A 129 × 29 × 33 C-H grid is used for its analysis. On each of the 33 H planes, there are 29 C curves, each defined by 129 points. The wing itself is defined by 80 cells in the chordwise direction and 24 cells in the spanwise direction.

The convergence to steady state, as monitored by the variation of the average residual, is found to be sensitive to the magnitude of VIS-4 when an adaptive dissipation scheme is used. This is to be expected because VIS-4 scales the fourth-difference terms, which provide the necessary background dissipation to suppress the high-frequency error components and thereby minimize aliasing errors. The convergence histories for three values of VIS-4, while VIS-2 is kept fixed at 1.0, are shown in Fig. 8. The converged results corresponding to the two higher values of VIS-4 were identical for all practical purposes. For coarser grids, smaller values of VIS-4 were found to be adequate.

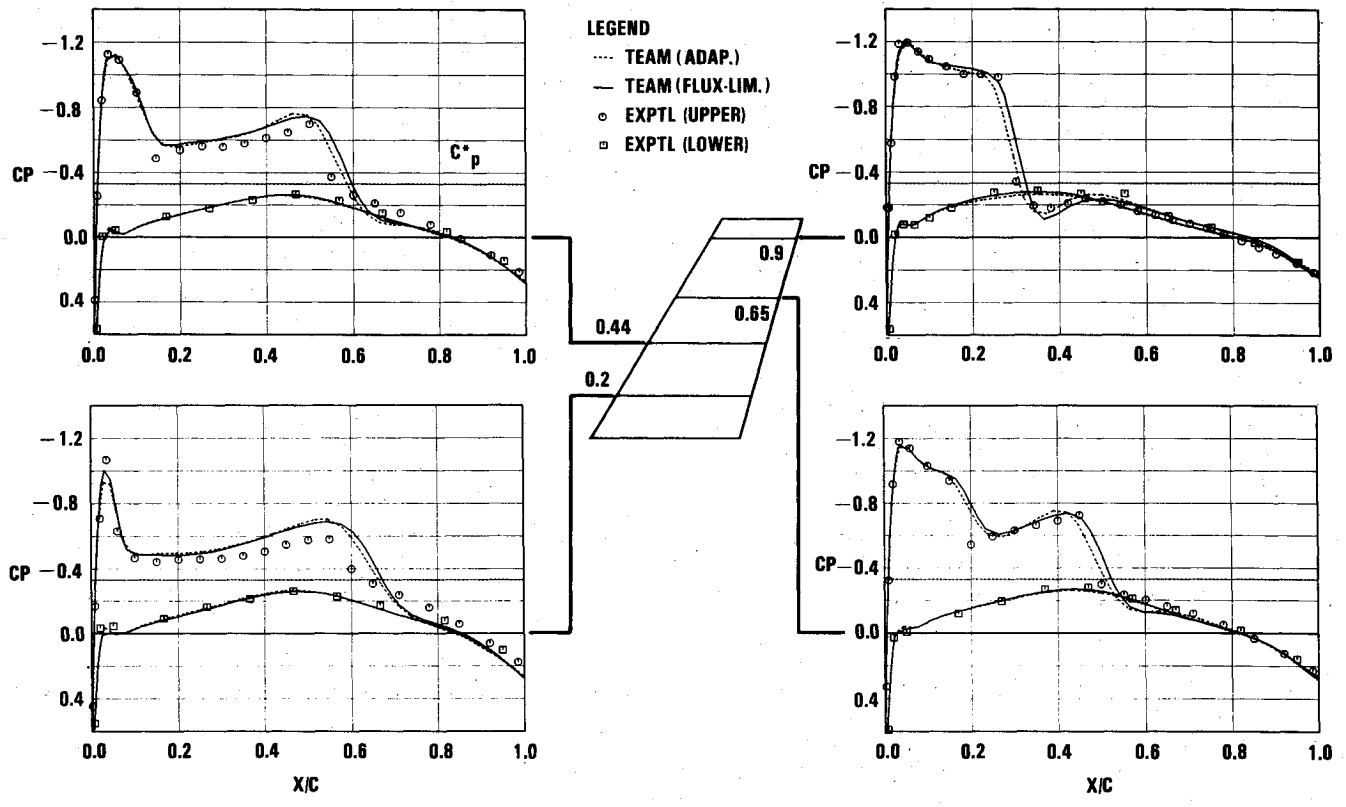

Fig. 9 Correlation of computed (TEAM) and measured surface pressures for ONERA M-6 Wing, $M = 0.84$, $\alpha = 3.06$ deg, $129 \times 29 \times 33$ C–H grid.

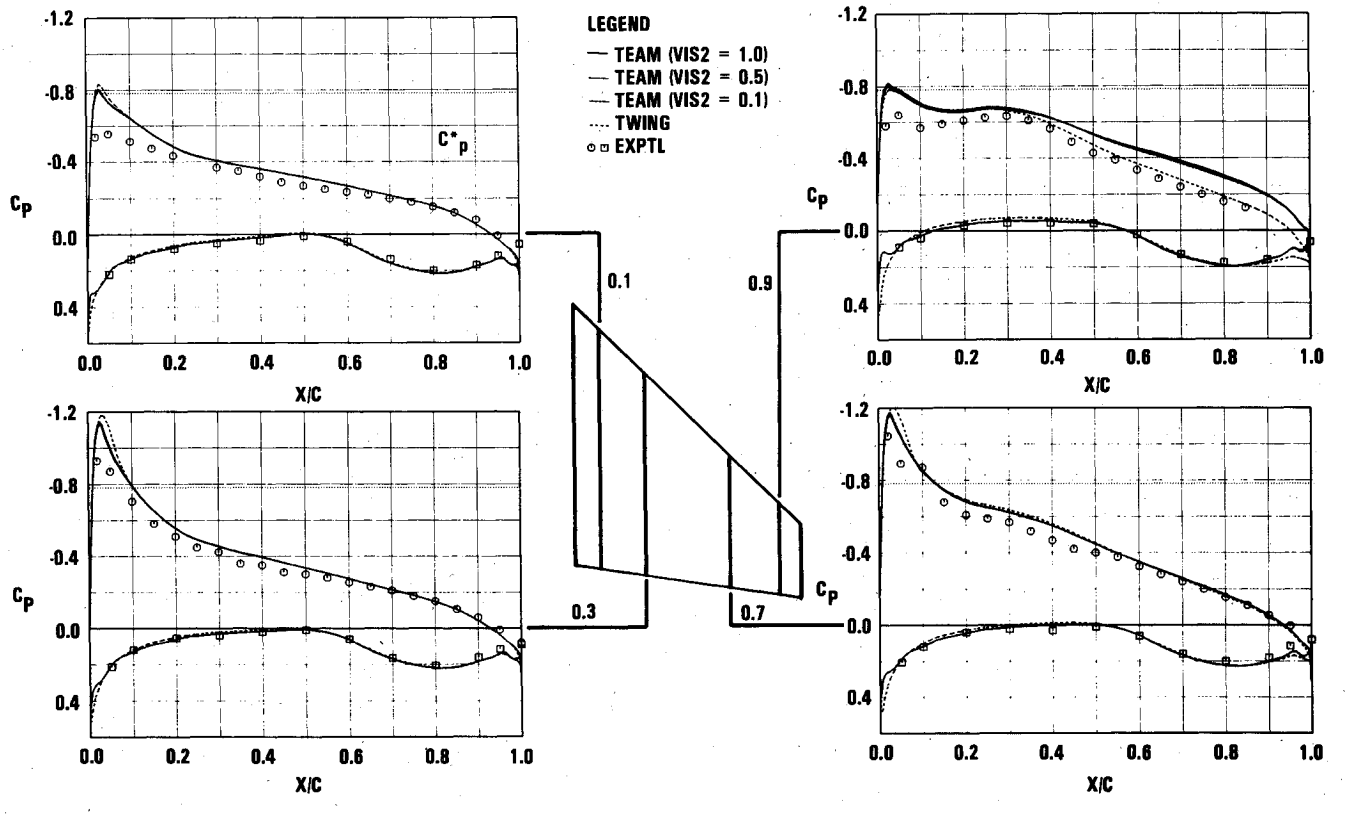

Fig. 10 Correlation of computed (TEAM and TWING) and measured surface pressures for Wing C, $M = 0.7$, $\alpha = 5$ deg, $127 \times 20 \times 27$ O–H grid.

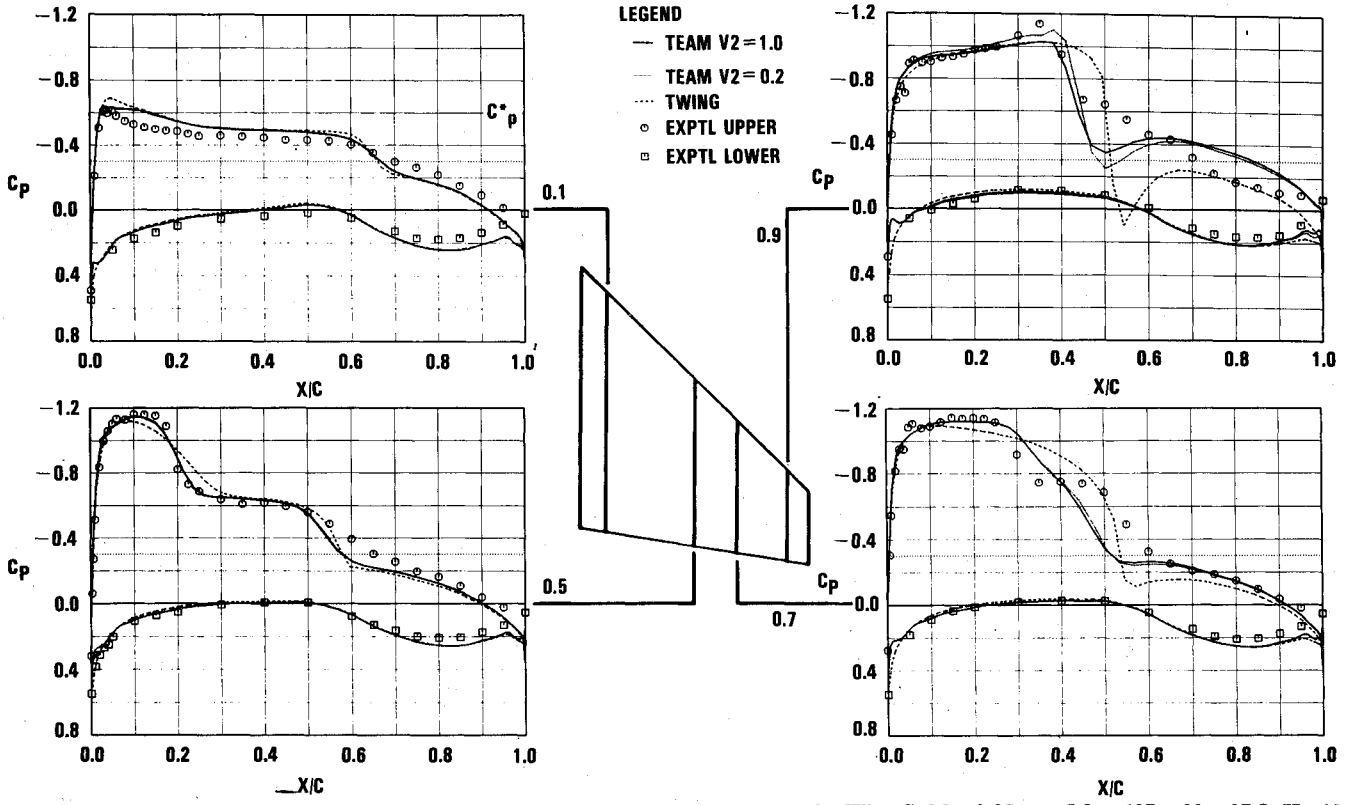

Fig. 11 Correlation of computed (TEAM and TWING) and measured surface pressures for Wing C, $M = 0.85$, $\alpha = 5$ deg, 127 × 20 × 27 O–H grid.

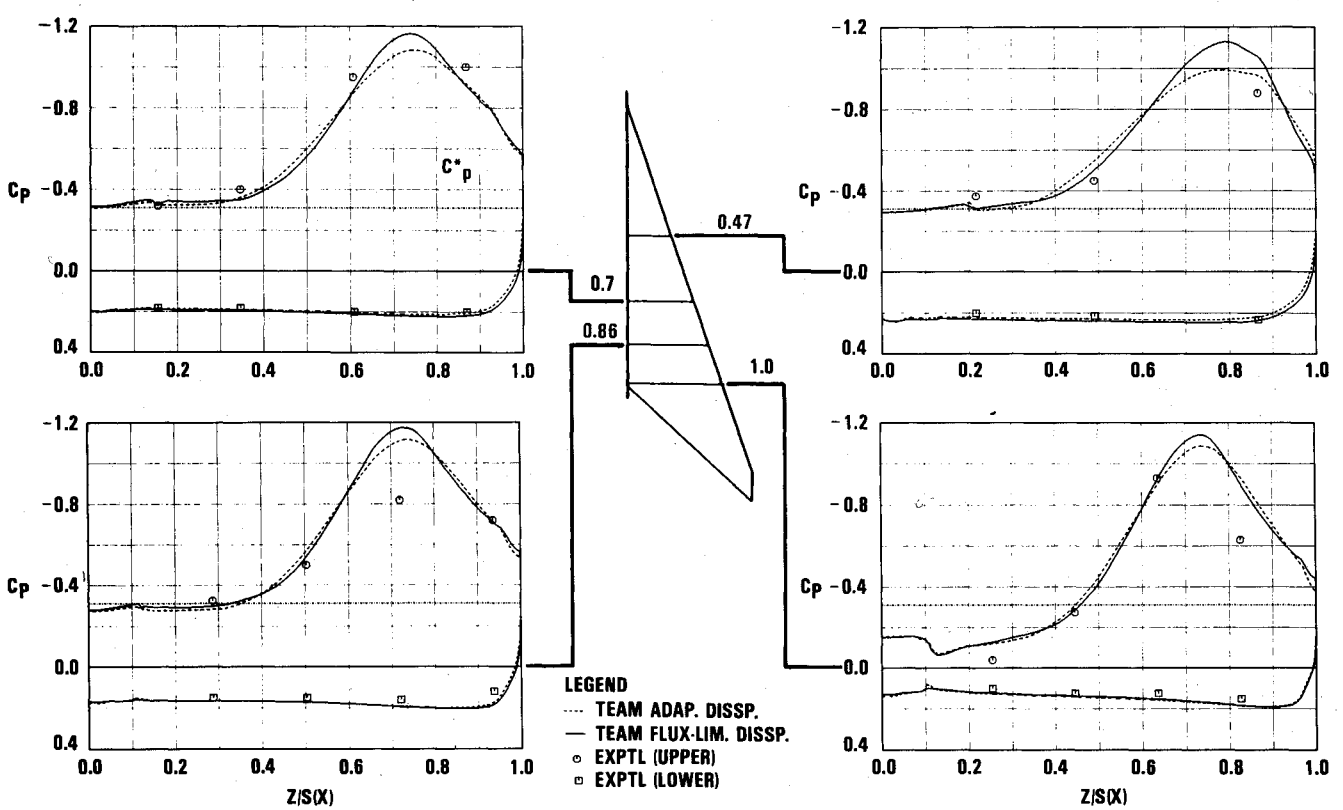

Fig. 12 Effect of numerical dissipation in Team on cross-plane pressure distribution for arrow wing-body configuration, $M = 0.85$, $\alpha = 15.8$ deg, 129 × 29 × 33 C–H grid.

A correlation of the computed and measured surface pressure distribution for 0.84 Mach number and 3.06-deg angle of attack is presented in Fig. 9. The computed results using adaptive dissipation and flux-limited dissipation agree quite well with each other and with the experimental data.

Wing C

The planform for Wing C is characteristic of a transonic maneuver fighter. The leading-edge sweep is 45 deg, the aspect ratio 2.6, and the taper ratio 0.3. A 127 × 20 × 27 O-H grid is used for its analysis. There are a total of 27 H planes. On each

plane, there are 20 O grids, each defined by 127 points. The wing is defined by 127 nodes in the chordwise direction and 19 nodes in the spanwise direction.

In Fig. 10, TEAM and TWING computations are correlated with experimental data[21] at 0.7 Mach number and 5-deg angle of attack. TEAM computations using flux-limited dissipation for three different values of VIS-2, namely, 0.1, 0.5, and 1.0, and VIS-4 = 1.5, are shown in Fig. 10. The results show very little sensitivity to changes in VIS-2. The TEAM and TWING computations agree well for all sections except the one near the tip.

The computed surface pressure distributions for 0.85 Mach number and 5-deg angle of attack are correlated with experimental data in Fig. 11. Fairly good agreement between computed and experimental data is seen at the inboard stations, but significant discrepancies are noticed at the outboard stations. These discrepancies may be attributed largely to strong viscid/inviscid interaction exhibited by the flow-field in the large-scale wind-tunnel test.[21] The TEAM computations using flux-limited dissipation for two values of VIS-2 (0.2 and 1.0) agree quite closely except for the station nearest the tip. Even there, the difference is small compared to the differences between the TEAM and TWING solutions. The TWING solutions show much stronger shocks at the outboard stations than those predicted by the TEAM solutions.

Arrow Wing-Body

The last set of results are for an arrow wing-body configuration.[22] The wing has a leading-edge sweep of 71.2 deg, a taper ratio of 0.1, and an aspect ratio of 1.4. All sections have sharp leading edges. This configuration is analyzed at 0.85 Mach number and 15.8-deg angle of attack, using a $129 \times 33 \times 33$ C-H grid. The wing is defined by 80 cells in the chordwise direction and 24 cells in the spanwise direction.

Computed surface pressure distributions at four cross-plane stations are compared with the measured data in Fig. 12. The two sets of computed results correspond to the two dissipation formulations: adaptive and flux-limited. Both solutions exhibit the characteristics of the leading-edge vortex flow, and the general flow features are similar. However, somewhat lower pressure levels are predicted by the flux-limited dissipation scheme, even though larger values of VIS-2 and VIS-4, 1.5 and 2.5, respectively, were required to obtain a converged solution compared to the adaptive dissipation scheme for which VIS-2 was 1.0 and VIS-4 was 1.5. Further investigation is required to evaluate fully the effect of the dissipation treatment on free-vortex flow simulations.

Concluding Remarks

In this paper, modifications to the finite-volume, explicit time-stepping solution algorithm of the three-dimensional Euler aerodynamic method (TEAM) are described. The areas of numerical dissipation and surface boundary conditions are specifically addressed. Four different schemes for estimating the dissipation terms near solid surfaces were explored, and their effect on the solution was examined in detail for NACA 0012 airfoil at 0.8 Mach number and zero angle of attack. The surface pressure distribution was not found to be too sensitive to the dissipative scheme. However, surface total pressure losses were different. Relatively large total pressure lossess were observed near the leading edge for all schemes. A more precise numerical implementation of the surface boundary condition was shown to reduce these losses significantly. Correlations of computed surface pressure distribution with experimental data were presented for two wings, ONERA M-6 and Wing C, and an arrow wing-body configuration. For Wing C, the TEAM computations were also compared with those of the TWING code on identical grids. These correlations attest to TEAM's capabilities for modeling transonic flows.

Acknowledgments

This investigation is partially funded by the U.S. Air Force under Contract F33615-84-C-3005. The authors wish to thank their colleague, Dr. Charles Olling, for valuable discussions regarding the surface-boundary-condition treatment. Thanks are due to Cray Research, Inc., Mendota Heights, Minnesota, for providing access to the Cray X-MP series of supercomputers that were used to obtain most of the results presented in this paper. Mr. Kent Misegades' help in this regard is gratefully acknowledged. The authors greatly appreciate the cooperation and assistance of Dr. Terry Holst of NASA Ames in making the TWING code available for the present investigation.

References

[1]Mehta, U. and Lomax, H., "Reynolds Averaged Navier-Stokes Computations of Transonic Flows—The State of the Art," *Progress in Astronautics and Aeronautics: Transonic Aerodynamics*, Vol. 81, edited by D. Nixon, AIAA, New York, 1982, pp. 297–375.

[2]Fujii, K. and Obayashi, S., "Practical Applications of New LU-ADI Scheme for the Three-dimensional Navier-Stokes Computation of Transonic Viscous Flows," AIAA Paper 86-0513, 1986.

[3]Raj, P., "A Multigrid Method for Transonic Wing Analysis and Design," *Journal of Aircraft*, Vol. 21, Feb. 1984, pp. 143–150.

[4]Holst, T. L. and Thomas, S. D., "Numerical Solution of Transonic Wing Flowfields," *AIAA Journal*, Vol. 21, June 1983, pp. 863–870.

[5]Caughey, D. A. and Jameson, A., "Progress in Finite-volume Calculations for Wing-Fuselage Combinations," *AIAA Journal*, Vol. 18, Nov. 1980, pp. 1281–1288.

[6]Jameson, A., "Transonic Flow Calculations," *Numerical Methods in Fluid Dynamics*, edited by H. J. Wirz and J. J. Smolderen, McGraw-Hill, New York, 1978.

[7]Erikson, L. L., Madson, M. D., and Woo, A. C., "Application of the TRANAIR Full-potential Code to Complete Configurations," ICAS-86-1.3.5, 1986.

[8]Jameson, A., Schmidt, W., and Turkel, E., "Numerical Solutions of the Euler Equations by Finite Volume Methods Using Runge-Kutta Time-Stepping Schemes," AIAA Paper 81-1259, 1981.

[9]Jameson, A. and Baker, T. J., "Solution of the Euler Equations for Complex Configurations," *Proceedings of the AIAA 6th Computational Fluid Dynamics Conference*, AIAA, New York, July 1983.

[10]Rizzi, A., "Damped Euler Equation Method to Compute Transonic Flow Around Wing-Body Combinations," *AIAA Journal*, Vol. 20, Oct. 1982, pp. 1321–1328.

[11]Sharble, R. C. and Raj, P., "An Algebraic Grid Generation Method Coupled with an Euler Solver for Simulating Three-dimensional Flows," AIAA Paper 83-1807, July 1983.

[12]Agarwal, R. K. and Deese, J. E., "Transonic Wing-Body Calculations Using Euler Equations," AIAA Paper 83-0501, Jan. 1983.

[13]Raj, P. and Sikora, J. S., "Free-Vortex Flows: Recent Encounters with an Euler Code," AIAA Paper 84-0135, Jan 1984.

[14]Raj, P., "Computational Simulation of Free-Vortex Flows Using an Euler Code," ICAS-84.3.1, Sept. 1984.

[15]Moitra, A., Turkel, E., and Kumar, A., "Application of a Runge-Kutta Scheme for High-Speed Inviscid Internal Flows," AIAA Paper 86-0104, Jan. 1986.

[16]Salas, M. D., Jameson, A., and Melnik, R. E., "A Comparative Study of the Nonuniqueness Problem of the Potential Equation," *Proceedings of the AIAA 6th Computational Fluid Dynamics Conference*, AIAA, New York, July 1983.

[17]Rizzi, A. and Eriksson, L. E., "Computation of Flow Around Wings Based on the Euler Equations," *Journal of Fluid Mechanics*, Vol. 148, 1984, pp. 45–71.

[18]Yu, N. J., Chen, H. C., Samant, S. S., and Rubbert, P. E., "Inviscid Drag Calculations for Transonic Flows," AIAA Paper 83-1928, July 1983.

[19]Jameson, A., "A Nonoscillatory Shock Capturing Scheme Using Flux Limited Dissipation," Princeton University, Princeton, NJ, MAE Rept. 1653, 1983.

[20]"Experimental Data Base for Computer Program Assessment," AGARD AR-138, May 1979.

[21]Keener, E. R., "Pressure-Distribution Measurements on a Transonic Low-Aspect Ratio Wing," NASA TM-86683, Sept. 1985.

[22]Manro, M. E., Manning, K. J. R., Hallstaff, T. H., and Rogers, J. T., "Transonic Pressure Measurements and Comparison of Theory to Experiment for an Arrow-Wing Configuration," NASA CR-2610, Aug. 1976.